applied optics

Computation of astigmatic and trefoil figure errors and misalignments for two-mirror telescopes using nodal-aberration theory

Guohao Ju,[1,2,*] Changxiang Yan,[1] Zhiyuan Gu,[1,2] and Hongcai Ma[1]

[1]Changchun Institute of Optics, Fine Mechanics and Physics, Chinese Academy of Sciences, Changchun, Jilin 130033, China
[2]University of Chinese Academy of Sciences, Beijing 100049, China
*Corresponding author: juguohao123@163.com

Received 14 January 2016; revised 21 March 2016; accepted 23 March 2016; posted 24 March 2016 (Doc. ID 257426); published 22 April 2016

In active optics systems, one concern is how to quantitatively separate the effects of astigmatic and trefoil figure errors and misalignments that couple together in determining the total aberration fields when wavefront measurements are available at only a few field points. In this paper, we first quantitatively describe the impact of mount-induced trefoil deformation on the net aberration fields by proposing a modified theoretical formulation for the field-dependent aberration behavior of freeform surfaces based on the framework of nodal aberration theory. This formulation explicitly expresses the quantitative relationships between the magnitude of freeform surfaces and the induced aberration components where the freeform surfaces can be located away from the aperture stop and decentered from the optical axis. On this basis, and in combination with the mathematical presentation of nodal aberration theory for the effects of misalignments, we present the analytic expressions for the aberration fields of two-mirror telescopes in the presence of astigmatic primary mirror figure errors, mount-induced trefoil deformations on both mirrors, and misalignments. We quantitatively separate these effects using the analytical expressions with wavefront measurements at a few field points and pointing errors. Valuable insights are provided on how to separate these coupled effects in the computation process. Monte Carlo simulations are conducted to demonstrate the correctness and accuracy of the analytic method presented in this paper.

OCIS codes: (110.6770) Telescopes; (080.1010) Aberrations (global); (220.1140) Alignment; (080.4228) Nonspherical mirror surfaces; (220.1080) Active or adaptive optics.

http://dx.doi.org/10.1364/AO.55.003373

1. INTRODUCTION

Due to the increase in the aperture size of the emerging generations of astronomical telescopes, their fabrication has become more and more difficult. Considering that they are more susceptible to dynamic thermal and gravitational variations, the challenges in supporting and aligning them have also increased. The effects of telescope errors resulting from incorrect optical manufacturing and deformations and misalignments due to gravity or thermal reasons can greatly degrade the observation performance of astronomical telescopes. Active optics systems present an efficient solution to these problems by sensing and correcting mirror figure errors and misalignments during observing periods [1]. Since its first application to the monolithic primary of the new technology telescope (NTT) [2] by European Southern Observatory, active optics systems have been widely used in astronomical telescopes in the last two decades. Among these are the 8 m class Very Large Telescope (the successor of NTT) [3], Gemini [4] and Subaru [5], the 4 m class Telescopio Nazionale Galileo [6], Southern Astrophysical Research telescope [7], the Visible and Infrared Telescope for Astronomy [8], the Advanced Technology Solar Telescope [9], and others [10,11].

In an active optics system the effects of different types of figure errors and misalignments need to be quantitatively separated before they can be actively corrected. Presently, numerical methods (such as nonlinear least-square fitting algorithms) are used in most active optics systems for the computation of these perturbations [12,13]. Nevertheless, these methods can hardly lead to any insight into the aberration-field dependencies that arise in the presence of the perturbations (mirror deformations and misalignments), and typically their computation accuracy is restricted by the nonlinearity of the Zernike coefficient sensitivity to the perturbation parameters [13]. Therefore, an analytic computation method tied closely to aberration theory is need. In this paper we will present an analytic computation method for some specific perturbation

conditions for two mirror telescopes, i.e., astigmatic figure error on the primary mirror (PM), trefoil deformations on both PM and secondary mirror (SM), and lateral misalignments of the SM. One of the main focuses is placed on how to separate and quantify the effect of the trefoil deformation on the SM in the presence of secondary-mirror misalignments. While some other perturbations, such as longitudinal misalignment and primary-mirror spherical figure error that can introduce defocus and spherical aberration, are usually controlled in any telescope based on active optics, this paper does not discuss them. These perturbations do not break the axial symmetry of the optical system, and their effects can be discussed separately using the current aberration theories for rotationally symmetric optical systems [14].

Nodal aberration theory (NAT), discovered by Shack [15] and developed by Thompson [16–20], can analytically describe the aberration fields of optical systems in the absence of rotational symmetry. This theory had been limited to optical imaging systems made of rotationally symmetric components that are tilted and/or decentered until the special case of an astigmatic optical surface located at the aperture stop (or pupil) was introduced into NAT by Schmid *et al.* [21]. Based on the characteristic astigmatic nodal properties in the presence of secondary-mirror misalignments and primary-mirror astigmatic figure error, the effects of misalignments and primary-mirror astigmatic figure error can be distinguished. Recently, Fuerschbach *et al.* [22,23] presented a more generalized theoretical formulation for the aberration behavior of non symmetric optical surfaces that could lie anywhere in the optical system. In this case the net aberration contribution becomes field-dependent, and many aberration components, each having unique field dependence, may arise. Fuerschbach *et al.* analyzed the impact of three-point mount-induced trefoil deformation on the net aberration fields. It was recognized that when an optical surface located away from the aperture stop is deformed by a mounting error in addition to the field-constant elliptical coma contribution, a field-conjugate, field-linear astigmatic contribution will also be introduced to the net aberration fields. This extension to NAT presents possibility for separating the impact of astigmatic and trefoil figure errors and misalignments while considering all the surfaces in the optical system.

While the theory proposed by Fuerschbach *et al.* can lead to valuable insights into the aberration behavior of freeform optical surfaces, however, the quantitative relationships between the magnitude of freeform surface and the induced aberration components were not explicitly described. Therefore, before this theory can be applicable to some cases involving quantitative calculation, it needs some modifications. In this paper we first propose a modified theoretical formulation for the aberration behavior of freeform surfaces with the aid of vector multiplication of NAT. We rediscuss the field-dependent behavior of freeform surfaces, aiming at providing more in-depth physical insights rather than pure mathematical manipulation. We explicitly express the quantitative relationships between the magnitude of freeform surfaces and the induced aberration components by introducing the scale factor for the beam footprint on the surface, which has its clear physical meaning. We study the effect of the decenter of freeform surface on the net aberration fields, and demonstrate that this effect can be seen as a shift of the aberration field for this freeform surface, which coincides with the conception of shifted aberration field center for the aspheric cap of an optical surface [24]. With this formulation we quantitatively express the effect of mount-induced trefoil deformation on the net aberration fields and make a comparison between the results of this work and the work of Fuerschbach *et al.* It is demonstrated that the scale factor for the beam footprint on the surface is indispensible in establishing the quantitative relationships between the magnitude of freeform surfaces and the induced aberration components. Based on the quantitative relationship, importantly, the induced field-conjugate, field-linear astigmatic component can be directly used to determine the orientation and magnitude of the trefoil deformation.

Since we can quantitatively express the impact of mount-induced trefoil figure error in an optical surface located away from the stop and decentered from the optical axis, we encounter another challenge: how to quantitatively separate the effects of an astigmatic primary-mirror figure error, trefoil deformations on both the primary and SM, and lateral misalignments of the SM. This case is very complicated because many factors couple with each other in determining the total aberration fields. The astigmatic aberration field consists of the contributions from the PM astigmatic figure error, SM trefoil deformation, and SM misalignments. The SM misalignments can further impact the aberration contribution from the SM trefoil deformation. Therefore, quantitatively separating the effects of astigmatic and trefoil figure errors and misalignments is not only important for active optics systems but also has some theoretical values. After we propose a modified theoretical formulation for the field-dependent aberration behavior of freeform surfaces to explicitly express the quantitative relationships between the magnitude of freeform surfaces and the induced aberration components, the mathematical representations for the aberration fields of optical systems in the presence of astigmatic and trefoil figure errors and misalignments can be obtained based on how we can compute these perturbation parameters. Monte Carlo computation simulations demonstrate that these mathematical representations of NAT can serve as a powerful tool in computing the perturbation parameters. In the computation process we also provide valuable insights into how to quantitatively separate different effects that couple together in determining the total aberration fields.

This paper is organized as follows. In Section 2 we quantitatively describe the impact of mount-induced trefoil deformation by explicitly expressing the quantitative relationships between the magnitude of freeform surfaces and the induced aberration components. In Section 3 we separate the effects of astigmatic figure error on the PM, trefoil deformations on both the PM and SM, and lateral misalignments of the SM. We quantify these perturbation parameters. In Section 4 computation simulations are conducted to verify the correctness and computation accuracy of the method presented in this paper. In Section 5 we summarize and conclude the paper.

2. QUANTITATIVE DESCRIPTION FOR THE IMPACT OF MOUNT-INDUCED TREFOIL DEFORMATION

Before quantitatively separating the effects of astigmatic figure error on the PM, trefoil deformations on both the PM and SM, and lateral misalignments of the SM, we need to quantitatively describe the impact of mount-induced trefoil deformation in an optical surface located away from the stop and decentered from the optical axis. This goal is achieved by rediscussing the field-dependent behavior of freeform surfaces and explicitly expressing the quantitative relationships between the magnitude of freeform surfaces and the induced aberration components where the freeform surfaces can be located away from the aperture stop and decentered from the optical axis.

A. Quantitative Formulation of the Field-Dependent Aberration Contribution from Freeform Surfaces

The freeform surface can be treated as a zero-power thin optical plate, and its contribution to the net aberration fields is not dependent on the angle of incidence, supposing a typically small field of view. Therefore if a freeform surface is located at the aperture stop, the beam footprint is the same for all field points. Therefore all field angles will receive the same aberration contribution from this surface.

It is well known that the wavefront aberration represents the optical path difference between the actual aberrated wavefront and a spherical reference wave. Since the freeform surface does not contribute optical power, it does not impact the optical path length for the spherical reference wave. Therefore, the aberration contribution of the freeform surface is equivalent to the optical-path difference it introduced to the actual aberrated wavefront.

A freeform optical surface can be defined by a conic plus a ϕ-polynomial (Zernike polynomial) overlay. However, in this paper, the term freeform surface particularly refers to the Zernike polynomial overlay, not including the base conic surface, in order to facilitate the discussion of the net aberration contributions from the Zernike polynomial overlay. Considering that the sag of freeform surfaces varies not only with the radial component, ρ, but also with the azimuthal component, ϕ, we suppose it is expressed as $z(\rho, \phi)$. Using the vector multiplication identity of NAT [17], $z(\rho, \phi)$ can be rewritten as the function of $\vec{\rho}$, $F(\vec{\rho})$, and $\vec{\rho} = \rho e^{i\phi}$. Thus when the freeform surface is located at the aperture stop, as shown in Fig. 1, the aberration contribution can be given by

$$W(\vec{\rho}) = (n' - n)F(\vec{\rho}), \tag{1}$$

where $W(\vec{\rho})$ represents the aberration contribution from the freeform surface, $\vec{\rho}$ denotes the normalized aperture vector. n and n' are the indices of refraction before and after the optical surface, respectively. It is important to realize that for optical systems consisting of mirrors $n = 1$, $n' = -1$ for odd times of reflection, and $n = -1$, $n' = 1$ for even times of reflection.

When the freeform optical surface is located away from the stop, the beam footprint for a certain field point only covers part of this surface so each field angle will receive a unique aberration contribution from the surface. Before formulating this field-dependent contribution we first consider a conceptual case that the freeform surface is still located at the aperture stop

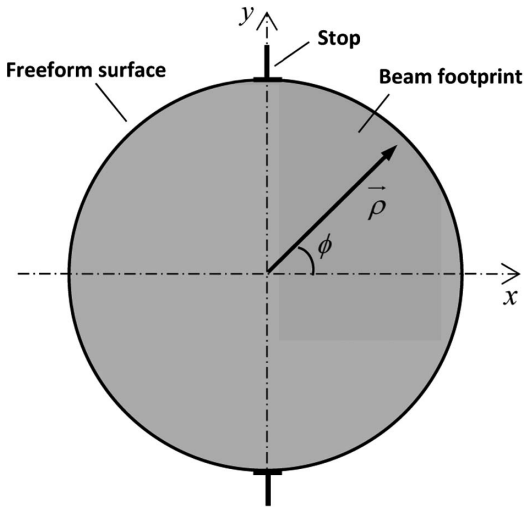

Fig. 1. Schematic representation for the case where the freeform surface is located at the aperture stop. In this case, the beam footprint is the same for different field points and covers the full surface.

but the aperture is scaled down by a factor of a and decentered by a normalized decentration vector $\vec{s}$, as illustrated in Fig. 2, where the small circle in gray represents the scaled and decentered aperture, and the large circle represents the previous on-axis full aperture of the freeform surface. In this case, only a portion of the freeform surface, which coincides with the scaled and decentered aperture, will contribute to the net aberration fields.

The relation between the coordinate of the scaled and decentered aperture and the previous on-axis full aperture can be given by

$$\vec{\rho} = a\vec{\rho}' + \vec{s}, \tag{2}$$

where $\vec{\rho}$ denotes the on-axis aperture vector normalized by the half-aperture size of the on-axis full aperture, $\vec{\rho}'$ represents the

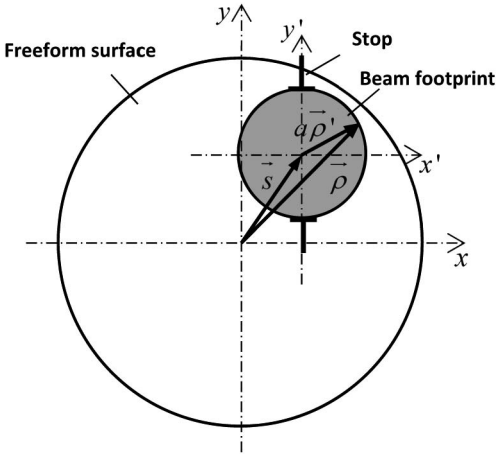

Fig. 2. Schematic representation for a conceptual case where the freeform surface is still located at the aperture stop but the stop is scaled down and decentered. In this case, the beam footprint is still the same for different field points compared with Fig. 1, but only covers part of the surface coinciding with the aperture stop.

scaled and decentered aperture vector normalized by the half-aperture size of the scaled aperture, $\vec{s}$ denotes the aperture decentration vector normalized by the radius of the on-axis full aperture, and a represents the scale factor of the scaled aperture relative to the full aperture.

In this case the optical path difference (OPD) introduced by the freeform surface can be given by

$$\mathrm{OPD}(\vec{\rho}) = (n' - n)F(\vec{\rho}), \qquad \vec{\rho} \in D, \tag{3}$$

where D represents the region of the scaled and decentered aperture. However, this expression cannot be directly seen as the aberration contribution induced by the freeform surface for this case. In that wave aberration is usually measured at exit pupil with a corresponding normalized aperture (pupil) coordinate. Since the aperture has been scaled and decentered, the OPD induced by the freeform surface should be measured in the scaled and decentered aperture coordinate. Therefore in this case the aberration contribution induced by the freeform surface can be expressed as

$$W(\vec{\rho}') = (n' - n)F(a\vec{\rho}' + \vec{s}), \tag{4}$$

where the coordinate transformation from the on-axis full aperture to the decentered and scaled aperture described by Eq. (2) has been used. It can be seen that the final measurement is done in the scaled and shifted aperture coordinate, and the aberration contribution of the freeform surface can thus be determined in this case.

For the case that the freeform surface is located away from the aperture stop, the beam footprint displaces on this surface, depending on field angle, and only covers part of the surface as illustrated in Fig. 3. This case parallels that the aperture stop is decentered and scaled down when the freeform surface is located at the aperture stop as discussed above, where the beam footprint also only covers part of the surface. While these two cases bear some similarities to each other, it is important to recognize the difference between them. In the case discussed above, the position for the beam footprint is field constant for the freeform surface located at the aperture stop. However, in this case, the position for the beam footprint is field dependent. Therefore, the ray bundles from different field points will receive different optical-path difference from the freeform surface, and the aberration contribution of the freeform surface becomes field dependent.

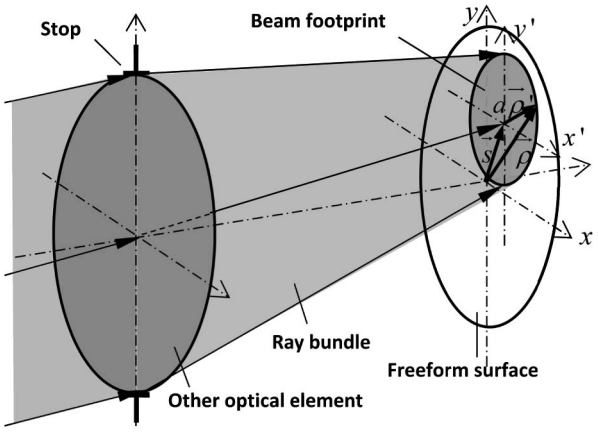

Fig. 3. Three-dimensional schematic representation for the case where the freeform surface is located away from the stop. Compared with Fig. 2, in this case the beam footprint for a certain field point still covers part of the freeform surface, but its position becomes field dependent.

We can refer to Eq. (4) to formulate the field-dependent aberration behavior when the freeform surface is located away from the aperture stop while taking the fact that the aperture decentration vector $\vec{s}$ is field dependent now into consideration. Furthermore, the aperture scale factor a and aperture decentration vector $\vec{s}$ are no longer conceptual quantities, they now have their clear physical meaning. The scale factor represents the ratio of the aperture size of the beam footprint relative to the freeform surface; the aperture decentration vector $\vec{s}$, which is field dependent, now locates the beam footprint on the surface. The half-aperture size of the beam footprint can be given by the paraxial marginal ray height on the surface, y, and the position of the off-axis beam footprint can be given by $\bar{y}\vec{H}$, the product of the paraxial chief ray height on the surface $\bar{y}$, and the normalized field vector $\vec{H}$. Therefore, the scale factor for the beam footprint can be given by

$$a = \frac{y}{R}, \tag{5}$$

where R represents the half-aperture size of the freeform surface. The normalized decentration vector for the beam footprint can be given by

$$\vec{s} = b\vec{H}, \tag{6}$$

with

$$b = \frac{\bar{y}}{R}. \tag{7}$$

Referring to Eq. (4), supposing the sag of the freeform surface can be given by $F(\vec{\rho})$, the field-dependent aberration contribution induced by the freeform surface can be expressed as

$$W(\vec{\rho}', \vec{H}) = (n' - n)F(a\vec{\rho}' + b\vec{H}), \tag{8}$$

where it can be seen that the final measurement is done in the scaled and shifted aperture coordinate, and the net aberration contribution of the freeform surface becomes field dependent. It is important to recognize that when the freeform surface is located at the aperture stop, $a = 1$, $b = 0$, and when it is located away from the stop $0 < a < 1, 0 < b < 1$. Therefore the approach proposed above can apply to both of the cases whether the freeform surface is located at the aperture stop or not. The only difference lies in the values of a and b.

When we determine the specific form of the field-dependent aberration components induced by the freeform surface using Eq. (8), vector multiplication identities of NAT [17] are typically needed to convert the expression $F(a\vec{\rho}' + b\vec{H})$ into a series of existing aberration types.

B. Impact of the Decenter of Freeform Surfaces on the Net Aberrations Fields

Previously, Fuerschbach *et al.* directly applied the conception of shifted aberration-field center for the aspheric cap of an optical surface in nodal aberration theory to discuss the effect of the decenter of the freeform surface on the net aberration fields [22]. While both of the freeform surface and the aspheric

departure can be seen as a zero-power thin plate, it is of great importance to recognize the difference that lies between them. The aspheric departure of an optical surface is rotationally symmetric, and the location of the point of rotational symmetry for its aberration field contributions is located at the intersection of the Gaussian image plane with the line connecting the aspheric vertex and the local entrance pupil of the surface; however, for freeform surfaces no such rotational symmetry exists. Therefore, directly following the method used in [24] for the decenter of an aspheric cap of an optical surface to discuss the effect of the decenter of freeform surfaces is not rigorous enough, even correct results can be obtained.

If the freeform surface is decentered from the optical axis, the position of the beam footprint for a certain field point relative to the optical axis will stay unchanged but the position relative to the decentered surface will change, as illustrated in Fig. 4. In this case the optical path difference introduced by the freeform surface for a certain field point will change. Therefore, a different aberration contribution will be induced by the freeform surface.

To account for this effect, the normalized decentration vector $\vec{s}$, which locates the off-axis portion on the freeform surface coinciding with the beam footprint for a certain field point, should be modified as

$$\vec{s} = b\vec{H} - \delta\vec{v}, \tag{9}$$

where $b\vec{H}$ denotes the normalized decentration vector for the off-axis portion relative to the optical axis, $\delta\vec{v}$ represents the normalized surface decentration vector that locates the position of the surface aspheric vertex, given by

$$\delta\vec{v} = \frac{\delta\vec{V}}{R}, \tag{10}$$

where $\delta\vec{V}$ gives the magnitude and orientation of the surface displacement with reference to the reference optical axis.

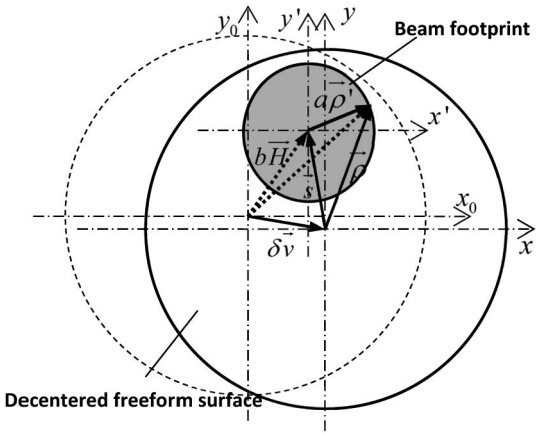

Fig. 4. Schematic representation for the case where the freeform surface is located away from the stop and decentered from the optical axis. The large circles in the dot line and solid line represent the freeform surface before and after it is decentered, respectively. In this case, the position of beam footprint is still field dependent compared with Fig. 3; however, due to the surface decentration a different portion of the surface will be illuminated by a certain field point, thus a different aberration contribution will be introduced by the surface.

The expression for the modified normalized-decentration vector for the beam footprint can be rewritten as

$$\vec{s} = b(\vec{H} - \vec{\sigma}_F), \tag{11}$$

where $\vec{\sigma}_F \equiv \delta\vec{V}/\bar{y}$. It can be seen that the field dependence for $\vec{s}$ displaces from a field center by a vector $\vec{\sigma}_F$. Since $\vec{s}$ determines the field dependence for the aberration contribution of the freeform surface (considering that $\vec{s}$ determines which portion of the freeform surface will contribute to the net aberration fields for a certain field point), the effect of the decenter of the freeform surface on the net aberration fields can be seen as an aberration field shift for this surface, and the shift of the aberration field is determined by $\vec{\sigma}_F$. This result coincides with the conception of shifted aberration field center for the aspheric cap of an optical surface [24], and can be seen as an extension of NAT to include decentered freeform surfaces.

We here define vector $\vec{H}_F \equiv \vec{H} - \vec{\sigma}_F$, which represents the effective aberration field height. By replacing $\vec{H}$ with $\vec{H}_F$ in Eq. (8), we can quantitatively map the impact of a decentered freeform surface on the net aberration fields.

Therefore, supposing the sag of the freeform surface can be given by $F(\vec{\rho})$, the field-dependent aberration contribution induced by the decentered freeform surface can be expressed as

$$W(\vec{\rho}', \vec{H}) = (n' - n)F(a\vec{\rho}' + b\vec{H} - \delta\vec{v}), \tag{12}$$

or using the conception of effective aberration field height,

$$W(\vec{\rho}', \vec{H}_F) = (n' - n)F(a\vec{\rho}' + b\vec{H}_F). \tag{13}$$

C. Quantitative Expression for the Impact of Mount-Induced Trefoil Deformation

After explicitly expressing the quantitative relationships between the magnitude of freeform surfaces and the induced aberration components we now can quantify the impact of mount-induced trefoil deformation. Comparisons are also made to the work of Fuerschbach *et al.* presented in [22]. Furthermore, it will be recognized that the field-conjugate, field-linear astigmatic term can be used to determine the magnitude and orientation of the trefoil deformation.

Current generations of telescopes often consist of large mirrors that are relatively thin for weight and thermal reasons. These mirrors can easily bend in trefoil, especially if there are three mounts supporting them. In either the measured or simulated case, Zernike polynomials are often used to fit deformations to optical surfaces. Therefore, surface deformation is typically quantified based on the values of its Fringe-Zernike coefficients. Trefoil deformation corresponds to the Fringe-Zernike polynomial terms Z_{10} and Z_{11} given by [25]

$$F_{333}(\rho, \phi) = {}_FC_{10}\rho^3 \cos(3\phi) + {}_FC_{11}\rho^3 \sin(3\phi), \tag{14}$$

where $F_{333}(\rho, \phi)$ represents the trefoil deformation, ${}_FC_{10}$ and ${}_FC_{11}$ are the corresponding Fringe-Zernike coefficient values. ρ is the normalized radial coordinate, and ϕ represents the azimuthal angle in the exit pupil. In optical testing, the Fringe-Zernike set is described in a right-handed coordinate system with ϕ measured counter-clockwise from the $\hat{x}$-axis.

Equation (14) can be rewritten in vector form using the vector multiplication identity of NAT [17] given by

$$F_{333}(\vec{\rho}) = \begin{bmatrix} {}_FC_{10} \\ {}_FC_{11} \end{bmatrix} \cdot (\vec{\rho})^3. \quad (15)$$

In case a trefoil deformation exists on the surface located at the aperture stop, the aberration contribution is field constant. Referring to Eq. (1) it can be added to the total aberration as

$$W_{333}(\vec{\rho}) = \frac{1}{4} {}_F\vec{C}^3_{333} \cdot \vec{\rho}^3, \quad (16)$$

where ${}_F\vec{C}^3_{333}$ is a two-dimensional vector introduced by Fuerschbach *et al.* [22] that describes the magnitude and orientation of field-constant elliptical coma, which can be given by

$${}_F\vec{C}^3_{333} = 4(n' - n) \begin{bmatrix} {}_FC_{10} \\ {}_FC_{11} \end{bmatrix}. \quad (17)$$

The introduction of ${}_F\vec{C}^3_{333}$ in this paper aims at facilitating the comparison between the results of this work and the work presented by Fuerschbach *et al.* and following the tradition of nodal aberration theory.

If the surface with trefoil deformation is now placed away from the aperture stop, only a portion of the surface, the position of which is field dependent, will contribute to the net aberration fields for a certain field point. Referring to Eq. (8) this field-dependent contribution can be given by

$$\begin{aligned} W_{333}(\vec{\rho}', \vec{H}) &= \frac{1}{4} {}_F\vec{C}^3_{333} \cdot (a\vec{\rho}' + b\vec{H})^3 \\ &= \frac{1}{4} \begin{bmatrix} a^3 {}_F\vec{C}^3_{333} \cdot (\vec{\rho}')^3 + 3a^2 b_F \vec{C}^3_{333} \vec{H}^* \cdot (\vec{\rho}')^2 \\ +3ab^2 {}_F\vec{C}^3_{333} (\vec{H}^*)^2 \cdot \vec{\rho}' + b^3 {}_F\vec{C}^3_{333} \cdot (\vec{H})^3 \end{bmatrix}, \end{aligned} \quad (18)$$

where the vector identity introduced in [17]

$$\vec{A} \cdot \vec{B}\vec{C} = \vec{A}\vec{B}^* \cdot \vec{C}, \quad (19)$$

has been used to convert the pupil dependence into existing aberration types, and $\vec{B}^*$ represents the conjugate vector of $\vec{B}$.

As can be seen from Eq. (18) three additional field-dependent aberration terms are generated in addition to the field-constant elliptical coma (trefoil) term, which parallels the result expressed by Eq. (14) in [22]. However, it is important to note that the magnitude of this field-constant elliptical coma is not equal to the magnitude of the surface trefoil deformation, a factor of a^3 must be accounted for. The second term is seen to be an astigmatic term based on the $\vec{\rho}^2$ aperture dependence whose magnitude has also been precisely described. The third and fourth terms are distortion and piston that do not affect the image quality but affect the mapping and phase.

If the surface with trefoil deformation, which is located away from the stop, is decentered from the optical axis, by replacing $\vec{H}$ with effective aberration field height $\vec{H}_F$, its aberration contribution can be given by

$$\begin{aligned} &W^{(\text{decentered})}_{333}(\vec{\rho}', \vec{H}_F) \\ &= \frac{1}{4} {}_F\vec{C}^3_{333} \cdot (a\vec{\rho}' + b\vec{H}_F)^3 \\ &= \frac{1}{4} \begin{bmatrix} a^3 {}_F\vec{C}^3_{333} \cdot (\vec{\rho}')^3 + 3a^2 b_F \vec{C}^3_{333} \vec{H}^*_F \cdot (\vec{\rho}')^2 \\ +3ab^2 {}_F\vec{C}^3_{333} (\vec{H}^*_F)^2 \cdot \vec{\rho}' + b^3 {}_F\vec{C}^3_{333} \cdot (\vec{H}_F)^3 \end{bmatrix}. \end{aligned} \quad (20)$$

Comparing Eqs. (18) or (20) with Eq. (14) in [22] presented by Fuerschbach *et al.*, we can see that they have similar form presenting the same field dependence for the induced aberration components. However, the quantitative relationships between the magnitude of trefoil deformation and the induced aberration components have not been explicitly described in Eq. (14) of [22].

It may seem that the only difference between the two results is the scale factor, and it is well known that the Zernike contribution of a sub-pupil is scaled relative to the Zernike contribution of a full pupil [26]. However, the scale factor in this paper is not just a meaningless quantity only used to perform mathematical manipulation; it has its definite and clear physical meaning. For a freeform surface located away from the aperture stop, the beam footprint for a certain field point covers part of the surface, so only the portion of the surface that coincides with the beam footprint will contribute to the net aberration fields for a certain field point. The scale factor represents the ratio of the aperture size of the beam footprint relative to the aperture size of the freeform surface. This parameter, combined with the field-dependent beam footprint decentration vector $\vec{s}$, also expressed as $b\vec{H}_F$, determines which portion of the freeform surface will contribute to the net aberration fields for a certain field point. For a matching freeform surface, a different scale factor will result in different aberration contribution from this surface. Therefore, to quantitatively map the impact of a freeform surface located away from the aperture stop, the scale factor must be considered and precisely determined.

It is also important to recognize that Eqs. (18) or (20) directly link the magnitude and orientation of the field-conjugate, field-linear astigmatic term to the trefoil deformation. Therefore, if we can determine the magnitude and orientation of this astigmatic term, the trefoil deformation can thus be characterized using the quantitative relationships presented in Eq. (20).

3. COMPUTATION OF ASTIGMATIC AND TREFOIL FIGURE ERRORS AND MISALIGNMENTS FOR TWO-MIRROR TELESCOPES

Since we can quantitatively describe the impact of mount-induced trefoil deformation in an optical surface located away from the stop and decentered from the optical axis, we can now begin to separate the effects of astigmatic and trefoil figure errors and misalignments when they couple together and compute these perturbation parameters. We will describe the aberration fields in terms of these perturbations using nodal aberration theory and demonstrate how to conduct the computation. Both the individual and coupled components will be discussed to facilitate an in-depth understanding of the computation process.

A. Case 1: Mount-Induced Trefoil Deformations on PM and SM

The first case discussed here is that trefoil deformations exist on the PM and SM of an aligned two-mirror telescope, assuming no other figure errors exist. The primary mirror serves as the aperture stop. In this case, the astigmatic aberration field of the system can be given by

$$W_{\text{AST3}} = \left(\frac{1}{2} W_{222} \vec{H}^2 + t \cdot {}_F\vec{C}^{3(\text{SM})}_{333} \vec{H}^* \right) \cdot \vec{\rho}^2, \quad (21)$$

where $t \equiv 3a_{SM}^2 b_{SM}/4$, a_{SM} and b_{SM} represent the aperture scale factor and aperture decentration factor for the beam footprint on the SM, respectively. ${}_F\vec{C}_{333}^{3(SM)}$ describes the magnitude and orientation of the field-constant elliptical coma introduced by the SM trefoil deformation when it is located at the stop. W_{222} represents the total astigmatic-wave aberration contribution.

According to vector multiplication [17] of NAT, Eq. (21) can be rewritten as

$$W_{AST3} = \begin{bmatrix} \frac{W_{222}}{2}(H_x^2 - H_y^2) + t \cdot {}_F\vec{C}_{333,x}^{3(SM)} H_x \\ + t \cdot {}_F\vec{C}_{333,y}^{3(SM)} H_y \end{bmatrix} \rho^2 \cos(2\phi) + \begin{bmatrix} W_{222} H_x H_y - t \cdot {}_F\vec{C}_{333,x}^{3(SM)} H_y \\ + t \cdot {}_F\vec{C}_{333,y}^{3(SM)} H_x \end{bmatrix} \rho^2 \sin(2\phi), \quad (22)$$

where the subscripts x, y represent the two components of a vector. Here $\hat{x}$-axis is used as the reference axis [27] and ϕ is measured counter clockwise from it, in accordance with the tradition of optical testing.

Since wavefront measurements typically provide the Zernike polynomial coefficients to the wavefront, the correspondence between the Seidel and Zernike coefficients can be utilized in computation of the unknowns. Though the exact correspondence between the Seidel coefficients and Zernike polynomials is generally an infinite sum, as discussed in detail by Tyson in [28], for two-mirror telescopes the high-order Zernike coefficients that are fitted against the wavefront are reasonably small so they can be ignored. In our paper the first 16 items of Fringe-Zernike coefficients are considered. According to this correspondence, referring to Eq. (22), we obtain

$$\begin{bmatrix} tH_x & tH_y \\ -tH_y & tH_x \end{bmatrix} \begin{bmatrix} {}_F\vec{C}_{333,x}^{3(SM)} \\ {}_F\vec{C}_{333,y}^{3(SM)} \end{bmatrix} = \begin{bmatrix} Z_{AST,x} \\ Z_{AST,y} \end{bmatrix}, \quad (23)$$

where

$$\begin{bmatrix} Z_{AST,x} \\ Z_{AST,y} \end{bmatrix} = \begin{bmatrix} C_5 - 3C_{12} - \frac{W_{222}}{2}(H_x^2 - H_y^2) \\ C_6 - 3C_{13} - W_{222} H_x H_y \end{bmatrix},$$

and C_i is the i-th Fringe-Zernike coefficient for the wave aberration at field (H_x, H_y). As can be seen from Eq. (23), there are two unknowns: ${}_F\vec{C}_{333,x}^{3(SM)}$ and ${}_F\vec{C}_{333,y}^{3(SM)}$. In order to solve them, wavefront measurement at a minimum of one off-axis field point is sufficient. If wavefront measurements at more than one field point are available, the two unknowns can be obtained by solving the least square solutions of the overdetermined equations. After ${}_F\vec{C}_{333}^{3(SM)}$ is solved, referring to Eq. (17) we can determine the Zernike coefficient values for the trefoil deformation on the SM, ${}_FC_{10}^{(SM)}$ and ${}_FC_{11}^{(SM)}$.

To determine the trefoil deformation on the PM, the total elliptical coma aberration field is needed, which can be expressed as

$$W_{Trefoil} = \frac{1}{4}\left(W_{333}\vec{H}^3 + {}_{TF}\vec{C}_{333}^{3}\right) \cdot \vec{\rho}^3, \quad (24)$$

where ${}_{TF}\vec{C}_{333}^{3} \equiv {}_F\vec{C}_{333}^{3(PM)} + a_{SM}^3 {}_F\vec{C}_{333}^{3(SM)}$, representing the total elliptical coma aberration contribution from the trefoil deformations on the two mirrors. W_{333} represents the total elliptical coma wave aberration contribution. For two-mirror telescopes with few freedoms the aberrations higher than third order are quite small, indicating that $W_{333} \approx 0$. Therefore, Eq. (24) can be rewritten as

$$W_{Trefoil} = \frac{1}{4}\,{}_{TF}\vec{C}_{333}^{3} \cdot \vec{\rho}^3. \quad (25)$$

Using vector multiplication of NAT, Eq. (25) can be rewritten as

$$W_{Trefoil} = \frac{1}{4}\begin{bmatrix} {}_{TF}\vec{C}_{333,x}^{3} \\ {}_{TF}\vec{C}_{333,y}^{3} \end{bmatrix} \cdot \begin{bmatrix} \rho^3 \cos(3\phi) \\ \rho^3 \sin(3\phi) \end{bmatrix}. \quad (26)$$

According to the relationship between Seidel coefficients and Zernike coefficients, we can obtain

$$\begin{bmatrix} {}_{TF}\vec{C}_{333,x}^{3} \\ {}_{TF}\vec{C}_{333,y}^{3} \end{bmatrix} = \begin{bmatrix} 4C_{10} \\ 4C_{11} \end{bmatrix}, \quad (27)$$

It can be seen that with wavefront measurement at only one field point, the total elliptical coma aberration contribution of the PM and SM can be determined. Since ${}_F\vec{C}_{333}^{3(SM)}$ can be solved using Eq. (23), consequently, ${}_F\vec{C}_{333}^{3(PM)}$ can be determined. Then by referring to Eq. (17) we can also obtain the Zernike coefficient values for the trefoil deformation on the PM, ${}_FC_{10}^{(PM)}$ and ${}_FC_{11}^{(PM)}$.

It is important to recognize that in this case the field-linear, field-conjugate astigmatic aberration field introduced by the mount-induced trefoil deformation on the SM can be directly used to determine the magnitude and orientation of the trefoil deformation on the SM, after the quantitative relationships between the magnitude of trefoil deformation and the induced aberration components are explicitly described. Then the magnitude and orientation of the trefoil deformation on the PM can be determined using the total elliptical coma aberration field. In this process, wavefront measurement at only one off-axis field point is enough.

B. Case 2: Mount-Induced Trefoil Deformations on PM and SM, Astigmatic Figure Error on the PM

The second case discussed here is that besides mount-induced trefoil deformations on the PM and SM, there exists astigmatic figure error on the PM due to manufacturing error and gravity or thermal reasons. In this case, the astigmatic aberration field of the system can be given by

$$W_{AST3} = \left(\frac{1}{2}W_{222}\vec{H}^2 + t \cdot {}_F\vec{C}_{333}^{3(SM)}\vec{H}^* + \frac{1}{2}{}_F\vec{B}_{222}^{2(PM)}\right) \cdot \vec{\rho}^2, \quad (28)$$

where ${}_F\vec{B}_{222}^{2(PM)}$ is a two-dimensional vector introduced by [21] that describes the magnitude and orientation of the astigmatic aberration contribution of the PM astigmatic figure error when the PM serves as the aperture stop, which is related to the astigmatic figure error of the PM by

$${}_F\vec{B}_{222}^{2(PM)} = 2(n' - n)\begin{bmatrix} {}_FC_5 \\ {}_FC_6 \end{bmatrix}, \quad (29)$$

where ${}_FC_5^{(PM)}$ and ${}_FC_6^{(PM)}$ are the Fringe-Zernike coefficient values for the astigmatic figure error of the PM.

According to vector multiplication of NAT, Eq. (28) can be rewritten as

$$W_{\mathrm{AST3}} = \begin{bmatrix} \frac{W_{222}}{2}(H_x^2 - H_y^2) + t \cdot {}_F\vec{C}^{3(\mathrm{SM})}_{333,x} H_x \\ +t \cdot {}_F\vec{C}^{3(\mathrm{SM})}_{333,y} H_y + \frac{1}{2} {}_F\vec{B}^{2(\mathrm{PM})}_{222,x} \end{bmatrix} \rho^2 \cos(2\phi) + \begin{bmatrix} W_{222} H_x H_y - t \cdot {}_F\vec{C}^{3(\mathrm{SM})}_{333,x} H_y \\ +t \cdot {}_F\vec{C}^{3(\mathrm{SM})}_{333,y} H_x + \frac{1}{2} {}_F\vec{B}^{2(\mathrm{PM})}_{222,y} \end{bmatrix} \rho^2 \sin(2\phi). \quad (30)$$

Using the relationship between Seidel coefficients and Zernike coefficients we get

$$\begin{bmatrix} tH_x & tH_y & \frac{1}{2} & 0 \\ -tH_y & tH_x & 0 & \frac{1}{2} \end{bmatrix} \begin{bmatrix} {}_F\vec{C}^{3(\mathrm{SM})}_{333,x} \\ {}_F\vec{C}^{3(\mathrm{SM})}_{333,y} \\ {}_F\vec{B}^{2(\mathrm{PM})}_{222,x} \\ {}_F\vec{B}^{2(\mathrm{PM})}_{222,y} \end{bmatrix} = \begin{bmatrix} Z_{\mathrm{AST},x} \\ Z_{\mathrm{AST},y} \end{bmatrix}. \quad (31)$$

where

$$\begin{bmatrix} Z_{\mathrm{AST},x} \\ Z_{\mathrm{AST},y} \end{bmatrix} = \begin{bmatrix} C_5 - 3C_{12} - \frac{W_{222}}{2}(H_x^2 - H_y^2) \\ C_6 - 3C_{13} - W_{222} H_x H_y \end{bmatrix}.$$

As can be seen from Eq. (31), there are four unknowns: ${}_F\vec{C}^{3(\mathrm{SM})}_{333,x}$, ${}_F\vec{C}^{3(\mathrm{SM})}_{333,y}$, ${}_F\vec{B}^{2(\mathrm{PM})}_{222,x}$, ${}_F\vec{B}^{2(\mathrm{PM})}_{222,y}$. In order to solve them, wavefront measurements at a minimum of two field points are sufficient. If wavefront measurements at more than two field points are available, the four unknowns can be obtained by solving the least square solutions of the overdetermined equations. After these four unknowns are solved, the Zernike coefficient values for the trefoil deformation on the SM and the astigmatic figure error on the PM can easily be determined.

Since ${}_F\vec{C}^{3(\mathrm{SM})}_{333,x}$, ${}_F\vec{C}^{3(\mathrm{SM})}_{333,y}$ can be solved using Eq. (31), the trefoil deformation on the PM can be determined with the total elliptical coma aberration field as discussed in Case 1.

The key observation obtained in this case is that while both the astigmatic figure error of PM and trefoil deformation of SM can contribute to the total astigmatic aberration field, their effects can directly be separated using wavefront measurements at a minimum of two field points. The main reason that underlies this observation is that the two astigmatic contributions have different field dependence.

C. Case 3: Mount-Induced Trefoil Deformations on PM and SM, Astigmatic Figure Error on the PM Lateral Misalignments of SM

For two mirror telescopes, PM, which typically serves as the aperture stop, is often chosen as the reference coordinate system leading to

$$\vec{\sigma}^{(\mathrm{sph})}_{\mathrm{PM}} = \vec{\sigma}^{(\mathrm{asph})}_{\mathrm{PM}} = \vec{0}, \quad (32)$$

where $\vec{\sigma}^{(\mathrm{sph})}_{\mathrm{PM}}$ and $\vec{\sigma}^{(\mathrm{asph})}_{\mathrm{PM}}$ are the field-center displacement vectors associated with the spherical base curve and the aspheric departure from the spherical base curve of the PM, respectively.

In the presence of SM misalignments, the corresponding SM aberration field-center displacement vectors $\vec{\sigma}^{(\mathrm{sph})}_{\mathrm{SM}}$ and $\vec{\sigma}^{(\mathrm{asph})}_{\mathrm{SM}}$ associated with the spherical base curve and the aspheric departure are generally non-zero. The relations between them and the misalignment parameters of the SM can be given by [24]

$$\vec{\sigma}^{(\mathrm{sph})}_{\mathrm{SM}} = \frac{1}{\overline{u}_{\mathrm{PM}}(1 + c_{\mathrm{SM}} d_1)} \begin{pmatrix} \mathrm{BDE}_{\mathrm{SM}} - c_{\mathrm{SM}} \mathrm{XDE}_{\mathrm{SM}} \\ -\mathrm{ADE}_{\mathrm{SM}} - c_{\mathrm{SM}} \mathrm{YDE}_{\mathrm{SM}} \end{pmatrix}, \quad (33)$$

$$\vec{\sigma}^{(\mathrm{asph})}_{\mathrm{SM}} = -\frac{1}{d_1 \overline{u}_{\mathrm{PM}}} \begin{pmatrix} \mathrm{XDE}_{\mathrm{SM}} \\ \mathrm{YDE}_{\mathrm{SM}} \end{pmatrix}, \quad (34)$$

where $\mathrm{XDE}_{\mathrm{SM}}$ and $\mathrm{YDE}_{\mathrm{SM}}$ are the SM vertex decenters in the x–z and y–z plane, respectively, and $\mathrm{BDE}_{\mathrm{SM}}$ and $\mathrm{ADE}_{\mathrm{SM}}$ are the SM tip-tilts in the x–z and y–z plane, respectively. $\overline{u}_{\mathrm{PM}}$ corresponds to the paraxial chief ray angle at the PM, d_1 is the distance from the PM to SM, c_{SM} corresponds to the curvature of the SM.

In the presence of misalignments, not only will the field dependence of particular aberration types be modified but also the image-plane displacement (boresight error or pointing error) will appear. Therefore, there exist certain relationships between pointing error and misalignment parameters. Pointing error can be quantified with the displacement of the field center from the reference axis, and the field center is located at the intersection of optical axis ray (OAR) with the image plane. Considering that the conic departure and freeform overlay can be seen as zero-power plates, they only impact aberration property and have no influence on the paraxial ray tracing. We can express the normalized pointing-error dependent on the aberration field-center $\vec{\sigma}^{(\mathrm{sph})}_{\mathrm{SM}}$ associated with the spherical base curve of the SM. Using the paraxial ray tracing of OAR [24], the normalized pointing-error can be given by

$$\vec{H}_{\mathrm{PE}} = -2 d_2 \overline{u}_{\mathrm{PM}} (1 + d_1 c_{\mathrm{SM}}) \vec{\sigma}^{(\mathrm{sph})}_{\mathrm{SM}} / \overline{h}_{\mathrm{IMG}}, \quad (35)$$

where $\vec{H}_{\mathrm{PE}}$ represents the pointing-error vector normalized by the paraxial image height $\overline{h}_{\mathrm{IMG}}$. d_2 denotes the distance from the SM to the paraxial image plane. Since the pointing error is typically available, this expression can be utilized to solve the misalignment parameters of the SM.

Now we begin to compute the astigmatic figure error on the PM, trefoil deformations on both PM and SM, and the lateral misalignments of the SM. In the presence of these perturbations, the astigmatic aberration field of the system can be given by

$$W_{\mathrm{AST3}} = \left(\frac{1}{2} W_{222} \vec{H}^2 - \vec{A}_{222} \vec{H} + t \cdot {}_F\vec{C}^{3(\mathrm{SM})}_{333} \vec{H}^* + \frac{1}{2} \vec{B}^2_{222} \right) \cdot \vec{\rho}^2, \quad (36)$$

where

$$\vec{A}_{222} = W^{(\mathrm{sph})}_{222,\mathrm{SM}} \vec{\sigma}^{(\mathrm{sph})}_{\mathrm{SM}} + W^{(\mathrm{asph})}_{222,\mathrm{SM}} \vec{\sigma}^{(\mathrm{asph})}_{\mathrm{SM}}, \quad (37)$$

$$\vec{B}^2_{222} = W^{(\mathrm{sph})}_{222,\mathrm{SM}} \left(\vec{\sigma}^{(\mathrm{sph})}_{\mathrm{SM}} \right)^2 + W^{(\mathrm{asph})}_{222,\mathrm{SM}} \left(\vec{\sigma}^{(\mathrm{asph})}_{\mathrm{SM}} \right)^2 + {}_F\vec{B}^{2(\mathrm{PM})}_{222} - 2t \cdot {}_F\vec{C}^{3(\mathrm{SM})}_{333} \vec{\sigma}^*_{F,\mathrm{SM}}, \quad (38)$$

where $W^{(\mathrm{sph})}_{222,\mathrm{SM}}$ and $W^{(\mathrm{asph})}_{222,\mathrm{SM}}$ denote the astigmatic aberration contribution from the base spherical curve and the aspheric departure of the SM, respectively. $\vec{\sigma}_{F,\mathrm{SM}}$ represents the shifted aberration field center for the freeform surface on the SM given by

$$\vec{\sigma}_{F,\mathrm{SM}} = \frac{1}{\bar{y}_{\mathrm{SM}}}\delta\vec{V}_{\mathrm{SM}} \equiv \frac{1}{\bar{y}_{\mathrm{SM}}}\begin{pmatrix}\mathrm{XDE}_{\mathrm{SM}}\\ \mathrm{YDE}_{\mathrm{SM}}\end{pmatrix}, \tag{39}$$

where $\bar{y}_{\mathrm{SM}}$ is the chief ray height on the SM. $\delta\vec{V}_{\mathrm{SM}}$ gives the magnitude and orientation of the decenter of SM with reference to the optical axis.

According to vector multiplication of NAT, Eq. (36) can be rewritten as

$$\begin{aligned} W_{\mathrm{AST3}} &= \begin{bmatrix} \frac{W_{222}}{2}(H_x^2 - H_y^2) - \vec{A}_{222,x}H_x + \vec{A}_{222,y}H_y \\ +t\cdot {}_F\vec{C}^{3(\mathrm{SM})}_{333,x}H_x + t\cdot {}_F\vec{C}^{3(\mathrm{SM})}_{333,y}H_y + \frac{1}{2}\vec{B}^{2}_{222,x} \end{bmatrix}\rho^2\cos(2\phi) \\ &+ \begin{bmatrix} W_{222}H_xH_y - \vec{A}_{222,y}H_x - \vec{A}_{222,x}H_y \\ -t\cdot {}_F\vec{C}^{3(\mathrm{SM})}_{333,x}H_y + t\cdot {}_F\vec{C}^{3(\mathrm{SM})}_{333,y}H_x + \frac{1}{2}\vec{B}^{2}_{222,y} \end{bmatrix}\rho^2\sin(2\phi). \end{aligned} \tag{40}$$

According to the relationship between Seidel coefficients and Zernike coefficients, we can obtain

$$\mathbf{H}_{\mathrm{AST}}\mathbf{M}_{\mathrm{AST}} = \mathbf{Z}_{\mathrm{AST}}, \tag{41}$$

where

$$\mathbf{H}_{\mathrm{AST}} = \begin{bmatrix} -H_x & -H_y \\ H_y & -H_x \\ tH_x & -tH_y \\ tH_y & tH_x \\ 1/2 & 0 \\ 0 & 1/2 \end{bmatrix}^T, \qquad \mathbf{M}_{\mathrm{AST}} = \begin{bmatrix} \vec{A}_{222,x} \\ \vec{A}_{222,y} \\ {}_{F333,x}C^{3(\mathrm{SM})} \\ {}_{F333,y}C^{3(\mathrm{SM})} \\ \vec{B}^{2}_{222,x} \\ \vec{B}^{2}_{222,y} \end{bmatrix},$$

$$\mathbf{Z}_{\mathrm{AST}} = \begin{bmatrix} Z_{\mathrm{AST},x} \\ Z_{\mathrm{AST},y} \end{bmatrix},$$

and

$$\begin{bmatrix} Z_{\mathrm{AST},x} \\ Z_{\mathrm{AST},y} \end{bmatrix} = \begin{bmatrix} C_5 - 3C_{12} - \frac{W_{222}}{2}(H_x^2 - H_y^2) \\ C_6 - 3C_{13} - W_{222}H_xH_y \end{bmatrix}.$$

As one can see, $\mathbf{M}_{\mathrm{AST}}$ is a matrix with six rows and one column. In order to solve these six unknowns, wavefront measurements at a minimum of three field points are sufficient. If wavefront measurements at more than three field points are available, the six unknowns can be obtained by solving the least-square solutions of the overdetermined equations. It also can be seen that the mount-induced trefoil deformation on the SM can directly be determined even if SM is misaligned.

Since $\vec{A}_{222,x}$, $\vec{A}_{222,y}$ can be solved using Eq. (41) with wavefront measurements at a minimum of three field points, Eqs. (35) and (37) can be utilized to solve the SM aberration field-center displacement vectors $\vec{\sigma}^{(\mathrm{sph})}_{\mathrm{SM}}$ and $\vec{\sigma}^{(\mathrm{asph})}_{\mathrm{SM}}$. On this basis, referring to the relations between these aberration field-center displacement vectors and the misalignment parameters of the SM given by Eqs. (33) and (34), misalignment parameters of the SM can be determined.

We can then compute the astigmatic figure error on the PM. Equation (38) can be rewritten as

$$\begin{aligned} {}_F\vec{B}^{2(\mathrm{PM})}_{222} &= \vec{B}^{2}_{222} + 2t\cdot {}_F\vec{C}^{3(\mathrm{SM})}_{333}\vec{\sigma}^{*}_{F,\mathrm{SM}} \\ &\quad - [W^{(\mathrm{sph})}_{222,\mathrm{SM}}(\vec{\sigma}^{(\mathrm{sph})}_{\mathrm{SM}})^2 + W^{(\mathrm{asph})}_{222,\mathrm{SM}}(\vec{\sigma}^{(\mathrm{asph})}_{\mathrm{SM}})^2], \end{aligned} \tag{42}$$

since all the variables on the right side of the equation have been solved, ${}_F\vec{B}^{2(\mathrm{PM})}_{222}$ can be determined. Referring to Eq. (29) we can determine the astigmatic figure error on the PM.

To determine the trefoil deformation on the PM, the total elliptical coma aberration field is needed, which can be given by [20]

$$W_{\mathrm{Trefoil}} = \frac{1}{4}[W_{333}\vec{H}^3 - 3(\vec{H}^2\vec{A}_{333}) + 3(\vec{H}\vec{B}^{2}_{333}) - \vec{C}^{3}_{333}]\cdot\vec{\rho}^3, \tag{43}$$

where

$$\begin{aligned} \vec{A}_{333} &= W^{(\mathrm{sph})}_{333,\mathrm{SM}}\vec{\sigma}^{(\mathrm{sph})}_{\mathrm{SM}} + W^{(\mathrm{asph})}_{333,\mathrm{SM}}\vec{\sigma}^{(\mathrm{asph})}_{\mathrm{SM}} \\ \vec{B}^{2}_{333} &= W^{(\mathrm{sph})}_{333,\mathrm{SM}}(\vec{\sigma}^{(\mathrm{sph})}_{\mathrm{SM}})^2 + W^{(\mathrm{asph})}_{333,\mathrm{SM}}(\vec{\sigma}^{(\mathrm{asph})}_{\mathrm{SM}})^2 \\ \vec{C}^{3}_{333} &= W^{(\mathrm{sph})}_{333,\mathrm{SM}}(\vec{\sigma}^{(\mathrm{sph})}_{\mathrm{SM}})^3 + W^{(\mathrm{asph})}_{333,\mathrm{SM}}(\vec{\sigma}^{(\mathrm{asph})}_{\mathrm{SM}})^3 - {}_{\mathrm{TF}}\vec{C}^{3}_{333}, \end{aligned} \tag{44}$$

with ${}_{\mathrm{TF}}\vec{C}^{3}_{333} \equiv {}_F\vec{C}^{3(\mathrm{PM})}_{333} + a^{3}_{\mathrm{SM}F}\vec{C}^{3(\mathrm{SM})}_{333}$, $W^{(\mathrm{sph})}_{333,\mathrm{SM}}$ and $W^{(\mathrm{asph})}_{333,\mathrm{SM}}$ denote the elliptical coma aberration contribution for the base spherical curve and the aspheric departure of the SM, respectively. For two-mirror telescopes with few freedoms, the aberrations higher than third order are quite small, indicating that $W_{333} \approx 0$, $W^{(\mathrm{sph})}_{333,\mathrm{SM}} \approx 0$ and $W^{(\mathrm{asph})}_{333,\mathrm{SM}} \approx 0$. Equation (43) can be rewritten as

$$W_{\mathrm{Trefoil}} = \frac{1}{4}{}_{\mathrm{TF}}\vec{C}^{3}_{333}\cdot\vec{\rho}^3. \tag{45}$$

Referring to the relationship between Seidel coefficients and Zernike coefficients, we obtain

$$\begin{bmatrix} {}_{\mathrm{TF}}\vec{C}^{3}_{333,x} \\ {}_{\mathrm{TF}}\vec{C}^{3}_{333,y} \end{bmatrix} = \begin{bmatrix} 4C_{10} \\ 4C_{11} \end{bmatrix}. \tag{46}$$

Wavefront measurements at one field point is enough to solve ${}_{\mathrm{TF}}\vec{C}^{3}_{333,x}$ and ${}_{\mathrm{TF}}\vec{C}^{3}_{333,y}$. Considering that ${}_FC^{3(\mathrm{SM})}_{333,x}$ and ${}_FC^{3(\mathrm{SM})}_{333,y}$ can be solved using Eq. (41), trefoil deformation on the PM can now be determined.

It can be concluded that with wavefront measurements at a minimum of three field points and pointing error data, the astigmatic figure error on the PM, the mount-induced trefoil deformations on the PM and SM, and the misalignment parameters of the SM can be directly computed utilizing NAT.

Four key points should be emphasized in this computation process. The first is that the field-linear, field-conjugate astigmatic term induced by trefoil deformation on the SM can directly be utilized to compute the trefoil deformation on the SM even when SM is decentered. Second, when SM is decentered, apart from the field-conjugate, field-linear astigmatic term, another field-constant astigmatic term can also be introduced into the aberration fields, which links directly to the trefoil deformation on the SM and the decenter parameters of SM. Third, the field-linear astigmatic term and pointing error can hardly be

impacted by figure errors. They are only dependent on misalignments of SM, which serve as the basis for the computation of misalignments of the SM. Last, misalignment-induced field-linear astigmatic contribution and field-constant astigmatic contribution have inherent relationships because they both have definite dependence on the aberration field-center displacement vectors for the SM, $\vec{\sigma}_{\mathrm{SM}}^{(\mathrm{sph})}$, and $\vec{\sigma}_{\mathrm{SM}}^{(\mathrm{asph})}$. Consequently, after these vectors are solved using the field-linear astigmatic term and pointing error, the misalignment induced field-constant astigmatic contribution can also be determined, which facilitates the computation of the astigmatic figure error on the PM. Therefore, when quantitatively separating different effects that couple together in determining the aberration fields, we should determine the magnitude and field dependence of each aberration term and reveal the inherent relationships between the aberration terms with different field dependence but induced by the same effect.

4. COMPUTATION SIMULATIONS

To verify the correctness and the computation accuracy of the computation approach proposed above, the most complicated case (case 3) presented in Section 3 will be simulated. The F/24, 2400 mm Hubble Space Telescope (HST) with ±0.10° field of view (a little larger than the nominal prescription) is used to conduct this simulation. The optical layout of this telescope is presented in Fig. 5, and its optical prescription, third-order aberration coefficients, and paraxial ray-trace data, which are needed in the computation, are given in Appendix A.

Wavefront measurements at three field points, (0°,0°), (0.07°,0.07°), and (0.07°,-0.07°), are used in the computation of the astigmatic PM figure error, trefoil deformations on both two mirrors, and SM lateral misalignments.

In the simulation process we first artificially introduce a set of astigmatic figure errors on the PM ($_FC_5^{(\mathrm{PM})}$, $_FC_6^{(\mathrm{PM})}$), trefoil deformations on the PM ($_FC_{10}^{(\mathrm{PM})}$, $_FC_{11}^{(\mathrm{PM})}$) and SM ($_FC_{10}^{(\mathrm{SM})}$, $_FC_{11}^{(\mathrm{SM})}$), and lateral misalignments of the SM ($\mathrm{XDE_{SM}}$, $\mathrm{YDE_{SM}}$, $\mathrm{ADE_{SM}}$, $\mathrm{BDE_{SM}}$) into the HST in the simulation software Code V. The resulting wavefronts at the three field points and pointing error can be obtained from simulation software. Utilizing the computation approach presented in the Section 3, these figure errors and misalignment parameters can be determined. The introduced

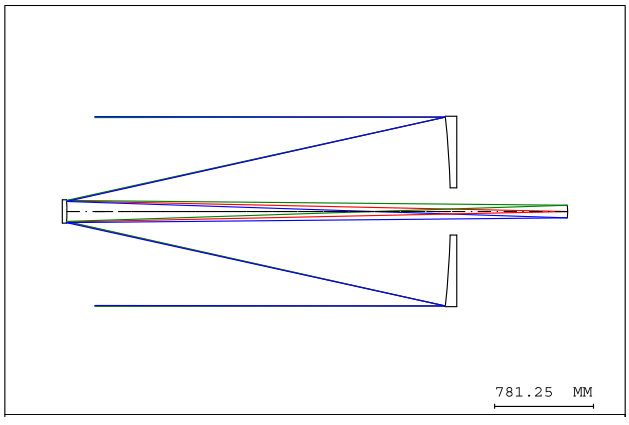

Fig. 5. Optical layout of the HST.

Table 1. Introduced (Row A) and Computed (Row B) Fringe-Zernike Coefficients for Figure Errors[a]

	$_FC_5^{(\mathrm{PM})}$	$_FC_6^{(\mathrm{PM})}$	$_FC_6^{(\mathrm{PM})}$	$_FC_{11}^{(\mathrm{PM})}$	$_FC_{10}^{(\mathrm{SM})}$	$_FC_{11}^{(\mathrm{SM})}$
A	0.2900	−0.2500	0.3700	−0.1900	−0.1200	−0.2800
B	0.2899	−0.2499	0.3658	−0.1897	−0.1200	−0.2801

[a]Fringe-Zernike coefficients are in λ ($\lambda = 500$ nm).

Table 2. Introduced (Row A) and Computed (Row B) Misalignment Parameters[a]

	$\mathrm{XDE_{SM}}$	$\mathrm{YDE_{SM}}$	$\mathrm{ADE_{SM}}$	$\mathrm{BDE_{SM}}$
A	0.2300	−0.1600	0.0100	0.0150
B	0.2299	−0.1599	0.0100	0.0150

[a]XDE and YDE are in mm while ADE and BDE are in degrees.

and computed figure error and misalignment parameters are presented in Tables 1 and 2, respectively.

It can be seen from the computation results presented in Tables 1 and 2 that except for trefoil deformation on the PM ($_FC_{10}^{(\mathrm{PM})}$, $_FC_{11}^{(\mathrm{PM})}$), the perturbation parameters can be computed with very high accuracy. The reasons why the trefoil deformation on the PM is computed with less accuracy may be that in the computation process we disregard the misalignment-induced elliptical coma aberration, and only the first 16 items of Fringe-Zernike coefficients are considered, which may be not enough for exactly expressing the correspondence between the Seidel coefficients and Zernike polynomials for elliptical coma in this perturbation condition.

Then we use the computed perturbation parameters to correct the system, i.e., adding a set of perturbation parameters that are the negative of the computed values into the system in the simulation software. The full field displays (FFDs) for the Fringe-Zernike coefficients of astigmatism (Z_5/Z_6), coma (Z_7/Z_8), and elliptical coma (Z_{10}/Z_{11}) before and after the correction are show in Fig. 6.

To further demonstrate the computation accuracy of the analytic method presented in this paper we will perform Monte Carlo computation simulations and make a comparison between the analytic method base on the NAT and the current numerical method based on nonlinear least square fitting algorithm (NLLSFA) [12,13]. The proper sensitivity matrix needed in NLLSFA was obtained in advance by numerically calculating the partial derivations of the wavefront Fringe-Zernike coefficients to the individual perturbations at the baseline design point. Four different cases will be considered in the Monte Carlo simulations. In Case 1, Case 2, and Case 3 the perturbation ranges increase progressively in turn but no measurement errors are considered. Case 4 has the same perturbation ranges as Case 3, however, it further includes 1% measurement errors in wavefront and boresight, i.e., a relative 1% of the measurement errors in plus or minus are randomly added to the wavefront Fringe-Zernike coefficients and boresight error read from the optical simulation software. The specific ranges for different perturbation parameters in each case are presented in Table 3.

For each case 100 perturbation states will be randomly generated following a uniform distribution and introduced into the optical-simulation software. For each randomly introduced perturbation state, the analytic method base on the NAT and the

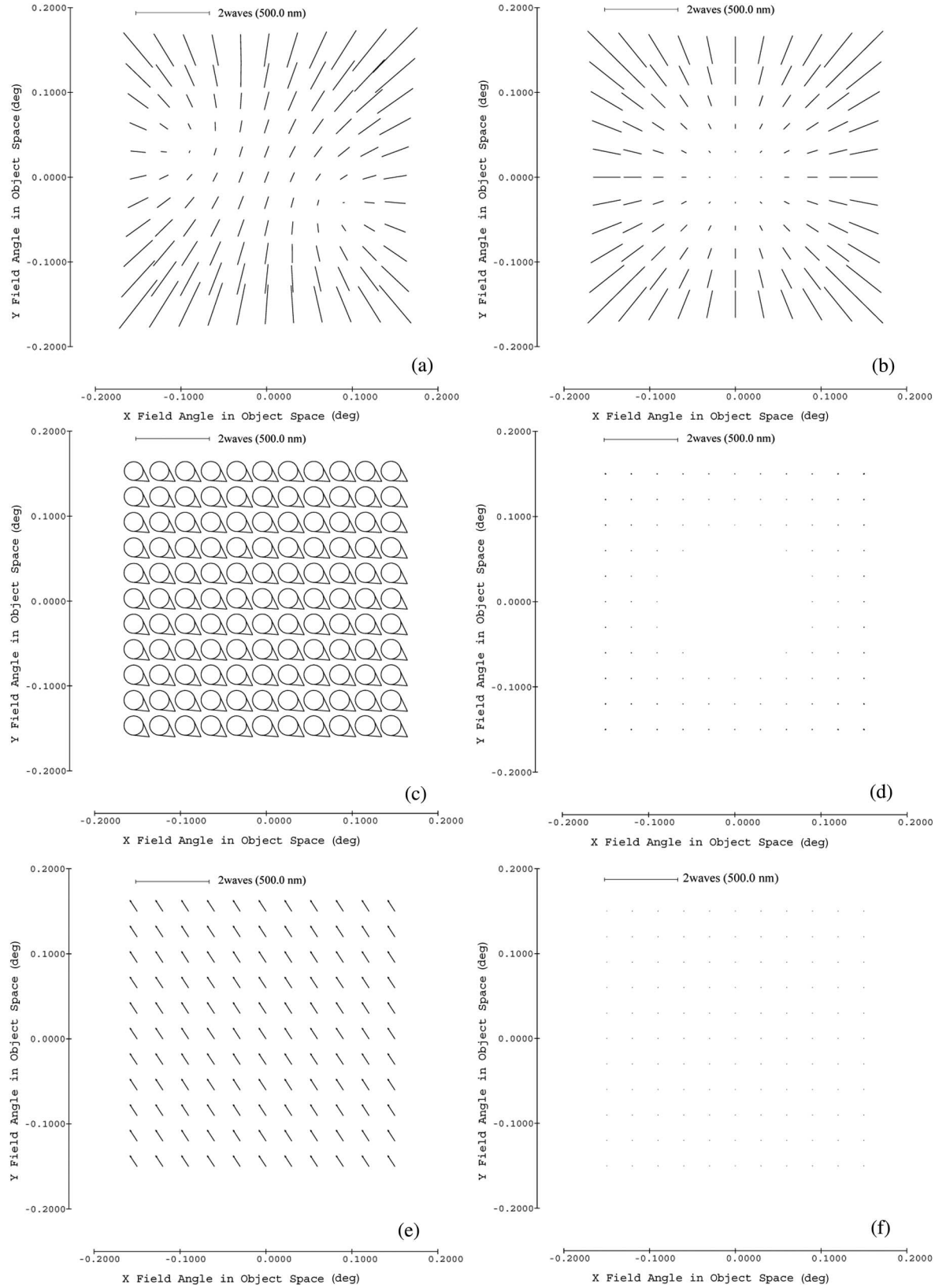

Fig. 6. (a) FFD for astigmatism (Z_5/Z_6) before correction, which includes contributions from primary mirror astigmatic figure error, SM trefoil deformation and misalignments. (b) FFD for the field quadratic astigmatism (Z_5/Z_6) after correction. (c) FFD for the misalignment-induced field-constant coma (Z_7/Z_8) before correction. (d) FFD for the field-linear coma (Z_7/Z_8) after correction. (e) FFD for the field-constant elliptical coma (Z_{10}/Z_{11}) before correction, which includes contributions from the trefoil deformations on both primary and SM. (f) FFD for elliptical coma (Z_{10}/Z_{11}) after correction, which is too small to be seen. After correction, the astigmatism, coma and elliptical coma aberration fields are restored very close to their nominal states.

Table 3. Four Different Cases Considered in the Monte Carlo Simulations[a]

	XDE_{SM}, YDE_{SM}	ADE_{SM}, BDE_{SM}	${}_FC_5^{(PM)}$, ${}_FC_6^{(PM)}$, ${}_FC_{10}^{(PM)}$, ${}_FC_{11}^{(PM)}$, ${}_FC_{10}^{(SM)}$, ${}_FC_{11}^{(SM)}$	Measurement Error
Case 1	[−0.1, 0.1]	[−0.01, 0.01]	[−0.1, 0.1]	\
Case 2	[−0.5, 0.5]	[−0.03, 0.03]	[−0.3, 0.3]	\
Case 3	[−1.0, 1.0]	[−0.05, 0.05]	[−0.5, 0.5]	\
Case 4	[−1.0, 1.0]	[−0.05, 0.05]	[−0.5, 0.5]	1%

[a]XDE and YDE are in mm, ADE and BDE are in degrees, and the Fringe-Zernike coefficients are in $\lambda(\lambda = 500$ nm).

Table 4. RMS Deviations Between the Introduced and Computed Values Using NAT and NLLSFA for Different Cases[a]

	Case 1		Case 2		Case 3		Case 4	
	NAT	NLLSFA	NAT	NLLSFA	NAT	NLLSFA	NAT	NLLSFA
XDE_{SM}	6.1×10^{-5}	1.7×10^{-3}	1.4×10^{-4}	1.2×10^{-2}	2.1×10^{-4}	4.1×10^{-2}	3.2×10^{-2}	3.8×10^{-2}
YDE_{SM}	4.2×10^{-5}	2.8×10^{-5}	1.3×10^{-4}	7.2×10^{-4}	2.1×10^{-4}	2.4×10^{-3}	3.1×10^{-2}	6.9×10^{-3}
ADE_{SM}	4.4×10^{-9}	2.7×10^{-6}	2.2×10^{-7}	7.0×10^{-5}	1.3×10^{-6}	2.3×10^{-4}	3.5×10^{-4}	5.9×10^{-4}
BDE_{SM}	5.0×10^{-9}	1.6×10^{-4}	2.3×10^{-7}	3.1×10^{-3}	1.1×10^{-6}	3.9×10^{-3}	3.5×10^{-4}	3.5×10^{-3}
${}_FC_5^{(PM)}$	1.4×10^{-5}	2.6×10^{-4}	4.3×10^{-5}	3.1×10^{-3}	7.1×10^{-5}	9.0×10^{-3}	2.8×10^{-3}	8.5×10^{-3}
${}_FC_6^{(PM)}$	1.3×10^{-5}	1.8×10^{-4}	4.0×10^{-5}	2.1×10^{-3}	7.2×10^{-5}	6.7×10^{-3}	3.0×10^{-3}	7.2×10^{-3}
${}_FC_{10}^{(PM)}$	6.0×10^{-4}	8.1×10^{-4}	1.9×10^{-3}	8.3×10^{-3}	3.3×10^{-3}	2.0×10^{-2}	3.5×10^{-3}	2.2×10^{-2}
${}_FC_{11}^{(PM)}$	6.9×10^{-4}	1.4×10^{-5}	1.8×10^{-3}	3.6×10^{-4}	2.7×10^{-3}	1.2×10^{-3}	3.7×10^{-3}	1.4×10^{-2}
${}_FC_{10}^{(SM)}$	2.3×10^{-5}	9.7×10^{-4}	5.1×10^{-5}	1.0×10^{-2}	7.2×10^{-5}	2.4×10^{-2}	1.8×10^{-2}	2.6×10^{-2}
${}_FC_{11}^{(SM)}$	1.6×10^{-5}	1.6×10^{-5}	4.5×10^{-5}	4.2×10^{-4}	7.0×10^{-5}	1.4×10^{-3}	1.7×10^{-2}	1.7×10^{-2}

[a]XDE and YDE are in mm, ADE and BDE are in degrees and the Fringe-Zernike coefficients are in λ ($\lambda = 500$ nm).

numerical method based on NLLSFA are used to calculate the perturbation parameters with boresight error and wavefront measurements at the three selected field points. Consequently, for each case we will obtain one set of randomly introduced perturbation parameters and two sets of computed values. Each set of data includes 100 perturbation states, and each perturbation state contains 10 individual perturbation parameters. The accuracy of the two methods is evaluated by the root mean square deviation (RMSD) between the introduced and computed values for each individual perturbation parameter, which is expressed as

$$\mathrm{RMSD}_i = \sqrt{\frac{1}{100}\sum_{n=1}^{100}[x_i(n) - X_i(n)]^2},$$

where $X_i(n)$ and $x_i(n)$ represent the introduced and computed set of values for the ith perturbation parameter, respectively. The computation results for different cases are presented in Table 4.

The computation results for Case 1, Case 2, and Case 3 show that the perturbation parameters can be computed with very high accuracy using NAT, which demonstrates the correctness of quantitative formulation for the impact of freeform surfaces located away from the stop and decentered from the optical axis, as well as the correctness of the computation method presented in this paper. By contrast, the computation accuracy of NLLSFA is relatively low. It is still important to recognize that the computation accuracy of NLLSFA declines obviously as the perturbations increase while the computation accuracy of NAT is almost unaffected. The main reason is that the NLLSFA is based on linear approximation of the nonlinear Zernike coefficient sensitivity to the perturbation parameters. When the perturbation ranges increase, the nonlinearity of Zernike coefficient sensitivity to perturbation parameters will also increase, and consequently, the accuracy of this linear approximation will decline.

However, comparing the computation results between Case 3 and Case 4, we can also find that the computation accuracy of NAT seems to be more sensitive to wavefront measurement errors than NLLSFA. In the presence of wavefront measurement errors, the computation accuracy of XDE_{SM}, YDE_{SM}, ${}_FC_{10}^{(SM)}$, and ${}_FC_{11}^{(SM)}$ decrease rapidly. This is mainly because the field-linear astigmatism term (induced by misalignments) and the field-linear, field-conjugate astigmatism term (induced by the trefoil deformation on the SM) are relatively small. It is hard to precisely determine them in the presence of wavefront measurement errors when wavefront measurements are available at only three field points. Even so, the computation accuracy of NAT is still higher than NLLSFA at the considered level of measurement errors. We also find that if wavefront measurements at more field points are available, the computation accuracy of NAT will be less sensitive to the measurement errors.

A more accurate computation of the perturbation parameters over larger perturbation ranges can mean a more efficient reconstruction of the wavefront. Therefore, nodal aberration theory presents possibility for improving the wavefront reconstruction performance of active optics systems.

5. CONCLUSION

In this paper we present an analytic method for quantitatively separating the effect of astigmatic and trefoil figure errors and misalignments for two-mirror telescopes using nodal aberration theory. We first present an in-depth discussion about the impact of the freeform surfaces on the net aberration fields. We

also propose a modified theoretical formulation for the field-dependent aberration behavior of freeform surfaces based on the framework of NAT to explicitly express the quantitative relationships between the magnitude of freeform surfaces and the induced aberration components where the conception of scale factor for beam footprint on the freeform surface is introduced and explained. We study the effect of the decenter of a freeform surface on the net aberration fields. It is demonstrated that this effect coincides with the conception of shifted aberration field center for the aspheric cap of an optical surface in NAT. With this modified formulation we can quantitatively describe the impact of mount-induced trefoil deformation in an optical surface located away from the stop and decentered from the optical axis. On this basis the mathematical representations for the aberration fields in the presence of PM astigmatic figure error, PM and SM trefoil deformations, and SM lateral misalignments are obtained, which can be directly utilized to compute these perturation parameters with wavefront measurements at a few field points and pointing errors. In the computation process some valuable insights are presented to help understand how to separate different effects that couple together in determining the total aberration fields. Monte Carlo computation simulations are further performed, which demonstrate the correctness and accuracy of the computation method presented in this paper. While this work is particularly for two-mirror telescopes, the theory, computation methods, and valuable insights presented in this paper can be extended to optical systems with more freedoms.

With the increase in the aperture size of the emerging generation of astronomical telescopes, active optics systems play a more and more important role in maintaining good observation performance. In active optics systems, figure errors and misalignment parameters need to be precisely computed before they are actively corrected. Therefore, this work can be utilized to help establish active compensation and alignment strategies for active optics systems.

APPENDIX A

This Appendix provides the optical prescription, third-order aberration coefficients and paraxial ray-trace data for the HST used in Section 4. See Tables 5–7.

Table 5. Prescription for the HST[a]

Surface	Type	Conic Constant	Radius	Thickness
PM (stop)	Conic	−1.00230	−11040.00	−4906.07
SM	Conic	−1.49686	−1358.00	6406.20
Image			−631.08	

[a]*Radius* and *Thickness* are in mm.

Table 6. Third-Order Astigmatic Aberration Coefficients of the HST[a]

	$W_{222,j}^{(\mathrm{sph})}$		$W_{222,j}^{(\mathrm{asph})}$
PM (stop)	0.7947		0
SM	−1.7003		1.5612
Sum		0.6556	

[a]Aberration coefficients are computed at a field angle of 0.1° at a wavelength of 0.5 μm.

Table 7. Paraxial Ray-Trace Data for the HST

	y (mm)	y (mm)
PM (stop)	1200.00	0
SM	133.46	8.56

Funding. National Natural Science Foundation of China (NSFC) (61205143).

REFERENCES

1. L. Noethe, "Active optics in modern, large optical telescopes," Prog. Opt. **43**, 1–69 (2001).
2. M. Tarenghi and R. N. Wilson, "The ESO NTT (new technology telescope): the first active optics telescope," Proc. SPIE **1114**, 302–313 (1989).
3. S. Stanghellini, P. Legrand, A. Baty, and T. Hovsepian, "Design and construction of the VLT primary mirror cell: support of the large, thin primary mirror," Proc. SPIE **2871**, 314–325 (1997).
4. L. Stepp, E. Huang, and M. Cho, "Gemini primary mirror support system," Proc. SPIE **2199**, 223–238 (1994).
5. M. Iye and K. Kodaira, "Primary mirror support system for the SUBARU telescope," Proc. SPIE **2199**, 762–772 (1994).
6. F. Bortoletto, D. Fantinel, R. Ragazzoni, C. Bonoli, and M. Alessandro, "Active optics handling inside Galileo telescope," Proc. SPIE **2199**, 212–222 (1994).
7. C. Neufeld, M. C. Zolcinski-Couet, M. Keane, and G. Ruthven, "The active primary mirror system for the SOAR telescope," Proc. SPIE **5489**, 870–880 (2004).
8. R. Bennet and F. Baine, "Active mirror support using pneumatic actuators," Proc. SPIE **5497**, 91–102 (2004).
9. M. Cho, R. Price, and I. Moon, "Optimization of the ATST primary mirror support system," Proc. SPIE **6273**, 62731E (2006).
10. P. L. Schechter, G. Burley, C. Hull, M. Johns, B. Martin, S. Schaller, S. A. Shectman, and S. C. West, "Active optics on the Baade 6.5m (Magellan I) telescope," Proc. SPIE **4837**, 619–627 (2003).
11. H. M. Martin, B. Cuerden, L. R. Dettmann, and J. M. Hill, "Active optics and force optimization for the first 8.4-m LBT mirror," Proc. SPIE **5489**, 826–837 (2004).
12. R. Upton, T. Rimmele, and R. Hubbard, "Active optical alignment of the Advanced Technology Solar Telescope," Proc. SPIE **6271**, 62710R (2006).
13. M. Liang, V. Krabbendam, C. F. Claver, S. Chandrasekharan, and B. Xin, "Active optics in large synoptic survey telescope," Proc. SPIE **8444**, 84444Q (2012).
14. J. C. Wyant and K. Creath, "Basic wavefront aberration theory for optical metrology," in *Applied Optics and Optical Engineering*, R. R. Shannon and J. C. Wyant, eds. (Academic, 1992), pp. 1–53.
15. R. V. Shack and K. P. Thompson, "Influence of alignment errors of a telescope system on its aberration field," Proc. SPIE **251**, 146–153 (1979).
16. K. P. Thompson, "Aberration fields in tilted and decentered optical systems," Ph.D. dissertation (University of Arizona, 1980).
17. K. Thompson, "Description of the third-order optical aberrations of near-circular pupil optical systems without symmetry," J. Opt. Soc. Am. A **22**, 1389–1401 (2005).
18. K. P. Thompson, "Multinodal fifth-order optical aberrations of optical systems without rotational symmetry: spherical aberration," J. Opt. Soc. Am. A **26**, 1090–1100 (2009).
19. K. P. Thompson, "Multinodal fifth-order optical aberrations of optical systems without rotational symmetry: the comatic aberrations," J. Opt. Soc. Am. A **27**, 1490–1504 (2010).
20. K. P. Thompson, "Multinodal fifth-order optical aberrations of optical systems without rotational symmetry: the astigmatic aberrations," J. Opt. Soc. Am. A **28**, 821–836 (2011).
21. T. Schmid, J. P. Rolland, A. Rakich, and K. P. Thompson, "Separation of the effects of astigmatic figure error from misalignments using nodal aberration theory (NAT)," Opt. Express **18**, 17433–17447 (2010).
22. K. Fuerschbach, J. P. Rolland, and K. P. Thompson, "Extending nodal aberration theory to include mount-induced aberrations with

application to freeform surfaces," Opt. Express **20**, 20139–20155 (2012).
23. K. Fuerschbach, J. P. Rolland, and K. P. Thompson, "Theory of aberration fields for general optical systems with freeform surfaces," Opt. Express **22**, 26585–26606 (2014).
24. K. P. Thompson, T. Schmid, O. Cakmakci, and J. P. Rolland, "Real-ray-based method for locating individual surface aberration field centers in imaging optical systems without rotational symmetry," J. Opt. Soc. Am. A **26**, 1503–1517 (2009).
25. R. W. Gray, C. Dunn, K. P. Thompson, and J. P. Rolland, "An analytic expression for the field dependence of Zernike polynomials in rotationally symmetric optical systems," Opt. Express **20**, 16436–16449 (2012).
26. L. Lundström and P. Unsbo, "Transformation of Zernike coefficients: scaled, translated, and rotated wavefronts with circular and elliptical pupils, " J. Opt. Soc. Am. A **24**, 569–577 (2007).
27. R. W. Gray and J. P. Rolland, "Wavefront aberration function in terms of R. V. Shack's vector product and Zernike polynomial vectors," J. Opt. Soc. Am. A **32**, 1836–1847 (2015).
28. R. K. Tyson, "Conversion of Zernike aberration coefficients to Seidel and high-order power-series aberration coefficients," Opt. Lett. **7**, 262–264 (1982).